SCIENCE CHINA
Technological Sciences

•Article•

June 2020 Vol.63 No.6: 1035–1044
https://doi.org/10.1007/s11431-019-1458-5

Bifurcation analyses and hardware experiments for bursting dynamics in non-autonomous memristive FitzHugh-Nagumo circuit

CHEN Mo, QI JianWei, WU HuaGan, XU Quan & BAO BoCheng*

School of Information Science and Engineering, Changzhou University, Changzhou 213164, China

Received July 29, 2019; accepted October 8, 2019; published online January 20, 2020

In this paper, a non-autonomous memristive FitzHugh-Nagumo (FHN) circuit is constructed using a second-order memristive diode bridge with LC network. For convenience of circuit implementation, an AC voltage source is adopted to substitute the original AC current stimulus. Stimulated by the slowly varying AC voltage source, the number, locations and stabilities of the equilibrium points slowly evolve with the time, which are thus indicated as the AC equilibrium points. Different sequences of fold and/or Hopf bifurcations are encountered in a full period of time series evolutions, leading to various kinds of chaotic or periodic bursting activities. To figure out the related bifurcation mechanisms, the fold and Hopf bifurcation sets are mathematically formulated to locate the critical bifurcation points. On this basis, the transitions between the resting and repetitive spiking states are clearly illustrated by the time series of the AC equilibrium points and state variables, from which Hopf/subHopf, Hopf/Hopf, and Hopf/fold bursting oscillations are identified in the specified parameter regions. Finally, based on a fabricated hardware circuit, the experimental measurements are executed. The results verify that the presented memristive FHN circuit indeed exhibits complex bursting activities, which enriches the family of memristor-based FHN circuits with bursting dynamics.

FitzHugh-Nagumo circuit, memristive diode bridge, bursting, AC equilibrium point

Citation: Chen M, Qi J W, Wu H G, et al. Bifurcation analyses and hardware experiments for bursting dynamics in non-autonomous memristive FitzHugh-Nagumo circuit. Sci China Tech Sci, 2020, 63: 1035–1044, https://doi.org/10.1007/s11431-019-1458-5

1 Introduction

In the biological nervous systems, bursting activities play important roles in information encoding and transmission, memory formation [1,2], and occurrence of neuronal disease [3]. Numerous mathematical neuronal models [4–8] have been established to promote theoretical investigations of the electrical activities in single and coupled neurons. The two-dimensional FitzHugh-Nagumo (FHN) model [9,10] is simplified from the four-dimensional Hodgkin-Huxley model for geometrical explanations of neuronal excitability and spiking under excitation. Many researches have been done on the significant and complex dynamical aspects of the FHN model. For example, Alidousti and Ghaziani [2] discussed various kinds of bursting activities in autonomous fractional-order FHN model. Baltanás and Casado [11] reported spontaneous bursting activities in FHN model subjected to quasi-monochromatic noise. Abbasian et al. [12] analyzed symmetric bursting activities in autonomous generalized FHN model. Besides, some specific dynamical behaviors, including chaos and bifurcation [13,14], noise or time delay influence [15–17], and synchronization characteristics [18,19], were also investigated by theoretical analyses, numerical simulations, and hardware experiments.

Due to the synaptic plasticity and non-volatile memory, memristor is becoming an excellent candidate for hardware

*Corresponding author (email: mervinbao@126.com)

implementations of neuromorphic circuits. At device levels, memristors have been proved to be able to emulate synaptic functions by storing analog synaptic weight or implementing synaptic learning rules [20]. Thus, memristors were used as essential building blocks for memristor crossbar-based neuromorphic computing or learning systems [20–22]. Besides, the effects of electromagnetic radiation [23–25] and coupling relationship between neuronal cells [26–29] can also be depicted by the memristive synapses. Inspired by these, some memristor-based FHN models have been proposed recently. Zhang et al. [24] used memristors with quadratic memductance to denote the nonlinear autapse or synapse current applied on isolated FHN model or occurred between FHN models in the chain network. Mvogo et al. [30] studied spatiotemporal formation of patterns in a diffusive FHN network where the modulation of magnetic flux on membrane potential was realized by memristor coupling. Ma et al. [31] investigated the effect of electric field in isolate neurons by introducing a new field variable E and distinct mode transitions of the electric activities were observed. Furthermore, by using a memristor synapse with non-smooth piecewise-linear memductance to realize the nonlinear membrane voltage function of the FHN model, Zhang and Liao [32,33] reported a chaotic non-autonomous FHN circuit and investigated the synchronization performances of memristive FHN circuits coupled by memristor synapse. Thereafter, Bao et al. [34] used an ideal memristor with hyperbolic tangent memductance to replace the memristor of refs. [32,33] and hidden extreme multistability was revealed and investigated through dimensionality reduction analyses. However, bursting activities and the related bifurcation mechanisms were rarely discussed in non-autonomous memristive circuits [35].

The bursting oscillation refers to oscillation transitions between the resting and repetitive spiking states caused by the modulation between the fast-scale and slow-scale variables. It has been found in a large variety of neuronal models [2,11,12,36–38] and nonlinear dynamical systems [39–43]. From the perspective of dynamical systems, the possible bifurcations and their role in the computational properties of bursting activities can be illustrated using geometrical methods [36]. For the autonomous systems, the fast-slow dissection method [40,43] can readily be applied for classifications of bursting activities. While for non-autonomous systems with a slowly varying periodic excitation, the exciting term is commonly regarded as a standalone control variable, then bifurcation mechanisms of the revealed bursting activities are explored using the so-called transformed phase portraits [39,41,42].

In this paper, aiming to perform quantitative analyses and experimental verifications of curious bursting activities in the non-autonomous memristive FHN model, a new neural model is constructed using the AC voltage source and second-order memristive diode bridge emulator. Driven by the slowly varying external force, different bursting activities are uncovered. Specially, the system trajectory passes a bifurcation point twice in a full period of the busting oscillation. Consequently, the transformed phase portrait overlaps together, leading to some difficulties in the bifurcation analyses. However, numerical simulations reveal that the characteristics of the AC equilibrium points provide abound information for identifying the bifurcation mechanisms of these bursting activities. It is proved to be an efficient method for theoretical analyses of dynamics in non-autonomous systems. Moreover, since the external stimulus is implemented using an AC voltage source, the revealed bursting activities are physically realized in a hardware circuit, which has rarely been reported in previous literature and could contribute to practical engineering applications of artificial neuromorphic circuits.

2 Non-autonomous memristive FHN circuit

The non-autonomous memristive FHN circuit is achieved by employing a second-order memristive diode bridge with LC network [40] to substitute the ideal memristor possessing non-smooth memductance in ref. [32] or smooth hyperbolic tangent memductance in ref. [34]. The circuit schematics of the main circuit and second-order memristive diode bridge emulator are presented in Figure 1(a) and (b), respectively. For convenience of experimental measurements, an AC voltage source $V_S=V_m\sin(2\pi ft)$, connected in series with a negative resistor R_1, is used to implement the external AC current excitation of the conventional FHN model.

2.1 Mathematical model

The voltage-current relation of the second-order memristive diode bridge emulator is given as [40]

$$i_M = 2I_S e^{-\rho v_0}\sinh(\rho v_C), \tag{1a}$$

$$\begin{cases} C_0 \mathrm{d}v_0/\mathrm{d}t = 2I_S\left[e^{-\rho v_0}\cosh(\rho v_C)-1\right]-i_0, \\ L_0 \mathrm{d}i_0/\mathrm{d}t = v_0. \end{cases} \tag{1b}$$

Four 1N4148 diodes are adopted to achieve the memristive diode bridge, thus the device parameters are determined as I_S=5.84 nA and ρ=10.31 V^{-1}. Based on eq. (1), the circuit equations of the non-autonomous memristive FHN circuit are established as

$$\begin{aligned} &C\mathrm{d}v_C/\mathrm{d}t = (V_S - v_C)/R_1 - i_L - 2I_S e^{-\rho v_0}\sinh(\rho v_C), \\ &L\mathrm{d}i_L/\mathrm{d}t = v_C + E - i_L R, \\ &C_0\mathrm{d}v_0/\mathrm{d}t = 2I_S\left[e^{-\rho v_0}\cosh(\rho v_C)-1\right]-i_0, \\ &L_0\mathrm{d}i_0/\mathrm{d}t = v_0. \end{aligned} \tag{2}$$

Denote

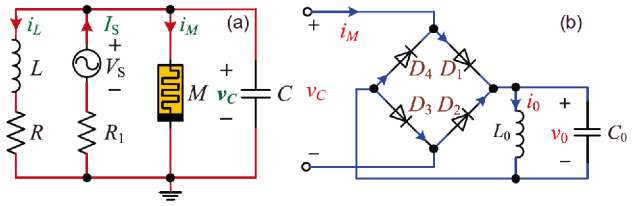

Figure 1 (Color online) Non-autonomous memristive FHN circuit. (a) Main circuit; (b) second-order memristive diode bridge emulator.

$$\begin{aligned} &x=\rho v_C,\ y=\rho R i_L,\ z=\rho v_0,\ u=\rho R i_0,\\ &w=A\sin(F\tau),\ t=RC\tau,\\ &A=\rho V_m,\ F=2\pi fRC,\ D=2\rho RI_S,\\ &k_r=R/R_1,\ k_c=C/C_0,\ l=R^2C/L,\ l_0=R^2C/L_0. \end{aligned} \tag{3}$$

The normalized model of eq. (2) is formulated as follows:

$$\begin{aligned} \dot{x}&=k_r(w-x)-y-De^{-z}\sinh x,\\ \dot{y}&=l(x-y),\\ \dot{z}&=k_c(De^{-z}\cosh x-D-u),\\ \dot{u}&=l_0 z. \end{aligned} \tag{4}$$

In eq. (4), there are the stimulus-related parameters A and F in the slowly varying variable w, diode-related parameter D, and other circuit-element-related control parameters k_r, k_c, l, and l_0. When the circuit element parameters of Figure 1 are assigned as V_m=1 V, f=0.32 kHz, C=10 nF, C_0=3.3 nF, L=15 mH, L_0=5 mH, R=1 kΩ, and R_1=−1.25 kΩ, these control parameters are calculated as

$$\begin{aligned} &A=10.31,\ F=0.02,\ D=1.204\times10^{-4},\\ &k_r=-0.80,\ k_c=3.03,\ l=0.667,\ l_0=2. \end{aligned} \tag{5}$$

In this case, a chaotic bursting pattern with LE_1=0.0124, LE_2=−0.0134, LE_3=−0.4901, and LE_4=−12.8254 is revealed. The phase portrait and time series are depicted in Figure 2(a) and (b), respectively. Obviously, the external forcing frequency F is much smaller than the natural frequency of system (4). So the slowly varying AC voltage stimulus modulates the fast variables and makes them switch between the resting and spiking states, leading to the occurrence of bursting oscillations.

Since the bursting activities caused by different bifurcation mechanisms are what we mainly concerned, k_r (i.e. the negative resistor R_1) and l (i.e. the inductor L) are selected as main control variables in later sections. These two parameters affect the bifurcation sequences encountered in a full period of time series evolutions, resulting in various kinds of chaotic or periodic bursting activities.

2.2 AC equilibrium point and stability

In non-autonomous systems, the equilibrium points are evolved with the variations of the external stimulus, which are thus indicated as the AC equilibrium points [44,45]. Letting $\dot{x}=\dot{y}=\dot{z}=\dot{u}=0$, the AC equilibrium point of system (4) is expressed as

$$E_{\rm AC}=(x_e,\ x_e,\ 0,\ D\cosh x_e-D), \tag{6}$$

where x_e is solved from the following equation:

$$F_0=(k_r+1)x_e+D\sinh x_e-k_r w=0. \tag{7}$$

The characteristic equation for evaluating the stability of $E_{\rm AC}$ is derived from the Jacobian matrix at $E_{\rm AC}$ as

$$\det(\mathbf{1}\lambda-\mathbf{J})=\lambda^4+a_3\lambda^3+a_2\lambda^2+a_1\lambda+a_0=0, \tag{8}$$

where

$$\begin{aligned} a_3&=(k_c+1)D\cosh x_e+k_r+l,\\ a_2&=(k_rk_c+k_cl+l)D\cosh x_e+(k_r+1)l+D^2k_c+k_cl_0,\\ a_1&=k_c(k_rl+l+l_0)D\cosh x_e+D^2k_cl+k_cl_0(k_r+l),\\ a_0&=k_cll_0(D\cosh x_e+k_r+1). \end{aligned} \tag{9}$$

Based on eqs. (7) and (8), the characteristics of $E_{\rm AC}$ can be readily evaluated. In addition, for the special case of w=0, system (4) has the DC equilibrium point characterized by

$$E_{\rm DC}=\left\{(x_e,x_e,0,D\cosh x_e-D)\middle|(k_r+1)x_e+D\sinh x_e=0\right\}. \tag{10}$$

When $k_r\geq-1$, there is only one DC equilibrium point $E_{\rm DC0}$=(0, 0, 0, 0); while for $k_r<-1$, there are three DC equilibrium points indicated as $E_{\rm DC0}$ and $E_{\rm DC\pm}$.

Figure 3(a) and (b) illustrate the trajectories of $E_{\rm AC}$ in the w-x_e plane for l=0.667 and k_r=−0.8/−1.2, respectively. The DC equilibrium points are marked using black dots. It can be seen that the number, locations, and stabilities of the AC equilibrium points vary along with the external stimulus w, from which the fold and Hopf bifurcation scenarios are readily figured out. And above all, the system orbit naturally evolves along the time-domain trajectory of the AC equilibrium point, which can provide distinct and abundant information for bifurcation analysis of the revealed bursting activities.

3 The fold and Hopf bifurcation sets

To locate the critical points of the fold and Hopf bifurcations in the time-domain trajectories of the AC equilibrium points, the formulations of the fold and Hopf bifurcation sets are mathematically deduced. On this basis, the mechanisms responsible for the bursting oscillations can be readily figured out.

3.1 The fold bifurcation set

Differentiate F_0 with respect to x_e. It yields

$$F_1=D\cosh\bar{x}+k_r+1=0, \tag{11}$$

which gives two zero points, written as

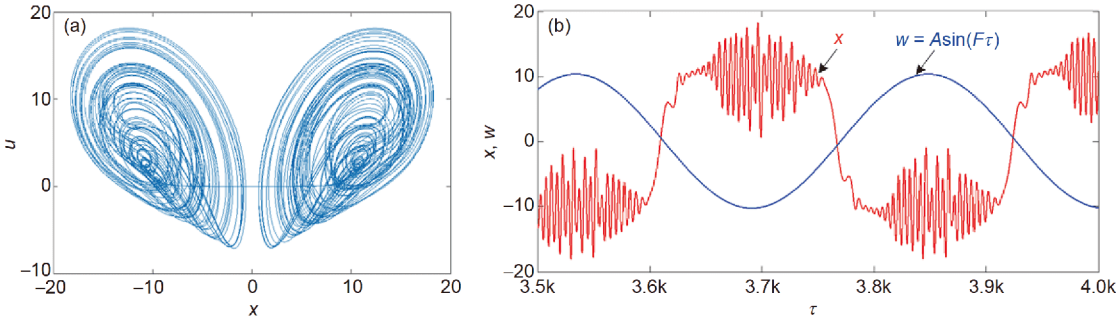

Figure 2 (Color online) Typical chaotic bursting pattern with k_r=−0.8 and l=0.667. (a) Phase portrait in the x-u plane; (b) time series of the fast state variable x and slowly varying stimulus w.

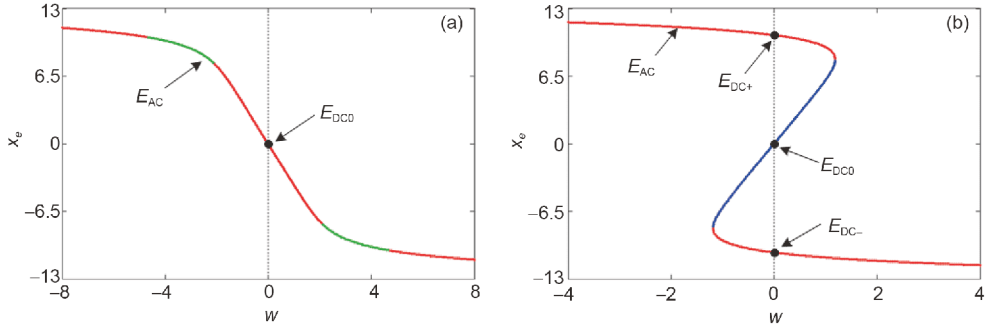

Figure 3 (Color online) AC and DC equilibrium points in the w-x_e plane, where the red, blue, and green colors represent unstable index-2 saddle-focus, unstable index-1 saddle-focus, and stable node-focus, respectively. (a) k_r=−0.8; (b) k_r=−1.2.

$$x_a = \operatorname{arccosh}\frac{-k_r-1}{D},\ x_b = -\operatorname{arccosh}\frac{-k_r-1}{D}. \tag{12}$$

When $k_r \le -1-D$, x_a and x_b have real roots, then F_0 reaches its extreme values, leading to the generation of the fold bifurcation (FB).

From the mathematical point of view, the FB refers to one zero eigenvalue [40,41], i.e. a_0=0 in eq. (8). Thus, the FB set can be deduced as

$$\text{FB:}\begin{cases} F_0 = (k_r+1)x_e + D\sinh x_e - k_r w = 0, \\ a_0 = k_c l l_0 (D\cosh x_e + k_r + 1) = 0, \end{cases} \tag{13}$$

and simplified as

$$\text{FB:}\pm\left[(k_r+1)\operatorname{arccosh}\frac{-k_r-1}{D} + D\sinh\left(\operatorname{arccosh}\frac{-k_r-1}{D}\right)\right] - k_r w = 0. \tag{14}$$

With reference to eq. (14), the FB set can be easily calculated with fixed control parameters D and k_r.

3.2 The Hopf bifurcation set

When the eigenvalues at E_{AC} pass across the imaginary axis, the Hopf bifurcation (HB) may occur. At the critical point of HB, eq. (8) possesses a pair of pure imaginary roots $\lambda=\pm j\omega$ ($\omega>0$) and the deviation of Re(λ) with respect to the varying system parameter should not equal to zero [46,47].

Substituting $\lambda=\pm j\omega$ ($\omega>0$) into eq. (8), we get

$$\begin{cases} a_1 - a_3\omega^2 = 0, \\ a_0 - (a_2 - \omega^2)\omega^2 = 0. \end{cases} \tag{15}$$

Eliminating ω in eq. (15), the necessary condition for HB is expressed as

$$\text{HB}: \begin{cases} F_0 = (k_r+1)x_e + D\sinh x_e - k_r w = 0, \\ a_1(a_3a_2 - a_1) - a_3^2 a_0 = 0. \end{cases} \tag{16}$$

Take k_r as a varying parameter, denote the critical HB point as c_H, and differentiate eq. (8) with respect to k_r. We get the following expression:

$$\frac{d\lambda}{dk_r} = -\frac{\lambda^3 + (k_c D\cosh x_e + l)\lambda^2 + (k_c l D\cosh x_e + k_c l_0)\lambda + k_c l l_0}{4\lambda^3 + 3a_3\lambda^2 + 2a_2\lambda + a_1}. \tag{17}$$

Put $\lambda(c_H)=\pm j\omega_H$ into eq. (17) and extract the real parts of the obtained equation. The sufficient condition for HB is deduced as

$$\left.\frac{dRe(\lambda)}{dc}\right|_{\lambda(c_H)=\pm j\omega_H} = \frac{b_1 b_3 + b_2 b_4}{b_1^2 + b_2^2} \neq 0, \tag{18}$$

where

$$\omega_{\mathrm{H}}=\sqrt{a_1/a_3},\ b_1=-2a_1,\ b_2=2\omega_{\mathrm{H}}\left(a_2-2\omega_0^2\right),$$
$$b_3=-(k_cD\cosh x_e+l)\omega_{\mathrm{H}}^2+k_cll_0, \tag{19}$$
$$b_4=\omega_{\mathrm{H}}\left(k_clD\cosh x_e+k_cl_0-\omega_{\mathrm{H}}^2\right).$$

To depict the HB set, the second implicit function of eq. (16) is first solved using MATLAB function to get the x_e values of each HB point. Then, the coordinates of the HB point and the corresponding w values can be readily obtained. These points are further verified using the sufficient condition described in eq. (18) to eliminate the points at which eq. (8) possesses pure imaginary roots but the eigenvalues do not pass the imaginary axis with the variation of k_r.

4 Bursting activities and bifurcation mechanisms

Based on the deduced FB and HB sets, as well as Izhikevich's classification scheme of bursting [36], the bursting activities of the non-autonomous memristive FHN circuit are revealed and identified. During the analyses, the parameters k_r and l are chosen as the main control variables and the initials are fixed as (0, 0, 0, 0).

4.1 Evolution of bursting activities

The variations of k_r and l lead to different combinations of FBs and HBs, and then change the exhibited dynamics of the non-autonomous memristive FHN circuit. Take l=0.667 and 3 as two examples. The FB and HB sets are depicted in the w-k_r plane, as shown in Figure 4. It can be found that for l=0.667, the HBs occur in the range of $-1.183\le k_r\le -0.628$ and FBs emerge within $-2\le k_r<-1$; while for l=3, the HBs are revealed in the region of $-2\le k_r\le -0.997$ and the FBs are found within $-2\le k_r<-1$. Note, to get better visual effect, only the essential regions of the bifurcation sets are depicted in Figure 4.

When l=0.667 is considered, four representative examples of k_r=−0.6, −0.72, −0.9, and −1.3 are selected to illustrate the dynamical evolutions. The time series of x overlapped with the x_e trajectories of E_{AC} are presented in Figure 5, in which the stabilities of E_{AC} are indicated using different colors as defined in Figure 3. At k_r=−0.6, there are two HB points located beyond the amplitude of the system orbit and the AC equilibrium points always behave as stable node-foci, as shown in Figure 5(a). Accordingly, the system orbit settles down to the resting state and a periodic spiking pattern is uncovered. Thereafter, the dynamics of system (4) gradually enters into the bursting activity at around k_r=−0.672. As depicted in Figure 5(b), a periodic bursting with negative largest Lyapunov exponent is observed at k_r=−0.72. The system orbit passes each of the four HB points twice in one bursting cycle, which is different from those reported in refs. [36,40,41]. When k_r is further decreased, the resting states of the bursting activities gradually reduce and finally become inconspicuous for $k_r<-0.85$. Then, the dynamics of system (4) turns into the spiking activity. Figure 5(c) illustrates a typical chaotic spiking with positive largest Lyapunov exponent uncovered at k_r=−0.9. Compared with Figure 5(b), the stable AC equilibrium point regions (indicated by the green lines) are too narrow to confine the large amplitude spiking states to the resting states. Thus, the spiking states are sustained in a whole cycle of the slow variable, leading to the symmetric chaotic spiking activity. At last, Figure 5(d) exhibits a chaotic spiking at k_r=−1.3. Under this parameter, no HBs exist, the stable AC equilibrium point regions completely disappear, and the upper and lower spiking oscillations are linked up via the FBs.

When l=3 is specified, the time series of x and x_e for k_r=−0.85, −1.0, −1.5, and −2.3 are presented in Figure 6. Similar with that illustrated in Figure 5, the dynamics of system (4) starts from periodic spiking, as shown in Figure 6(a), and gradually enters into bursting region within $-0.9\le k_r<-1.39$. Figure 6(b) illustrates a typical periodic bursting generated under k_r=−1.0. It should be noted that within $-0.9\le k_r\le -1$, two HPs induce the transitions between the resting and spiking states; while for $-1<k_r<-1.39$, two HPs and two FBs induce those oscillation state transitions. If k_r is further decreased, the regions where the AC equilibrium points behave as the stable node-foci are gradually narrowed. Consequently, the resting states, at which the orbit resides at the stable AC equilibrium points or a small amplitude oscillation, are shortened and finally vanished for $k_r<-1.39$. Thereafter, system (4) enters into the spiking region. Two representative spiking activities at k_r=−1.5 and −2.3 are plotted in Figure 6(c) and (d), respectively. In this parameter region, the system orbit simply oscillates around the unstable index-2 saddle-foci in the AC equilibrium trajectory, leading to the symmetric spiking activities. The existed HB and FB points do no exert any influences on the exhibited dynamics.

It is remarkable that the dynamical evolutions of Figure 6 are similar with those revealed in Figure 5, but the inner mechanisms are totally different.

4.2 Bifurcation analysis

As shown in Figure 2(a), the non-autonomous memristive FHN circuit operates in chaotic bursting pattern for k_r=−0.8 and l=0.667. To investigate the bifurcation mechanism, the time series of x, x_e (the x coordinate of the AC equilibrium point), and z are drawn in Figure 7(a), and the transformed phase portrait [41] in the w-x plane overlapped with the trajectory of E_{AC} is supplemented in Figure 7(b). With eq. (16), the four HBs are calculated as (w, x)=(∓4.7283, ±10.2638) and (w, x) =∓2.1128, ±7.7514), which are further

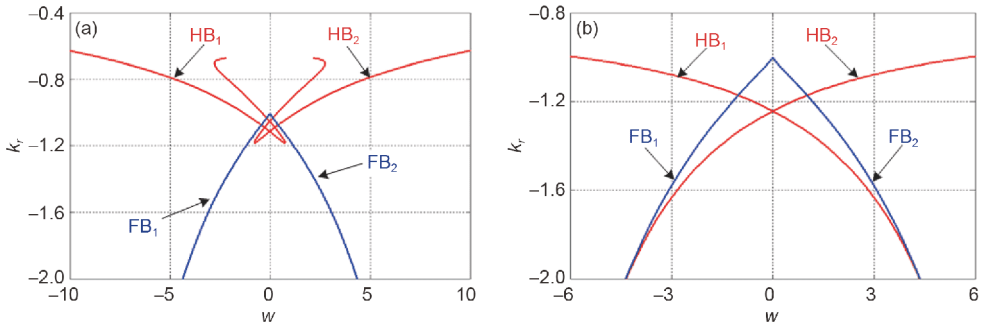

Figure 4 (Color online) HB and FB sets in the w-k_r plane. (a) l=0.667; (b) l=3.

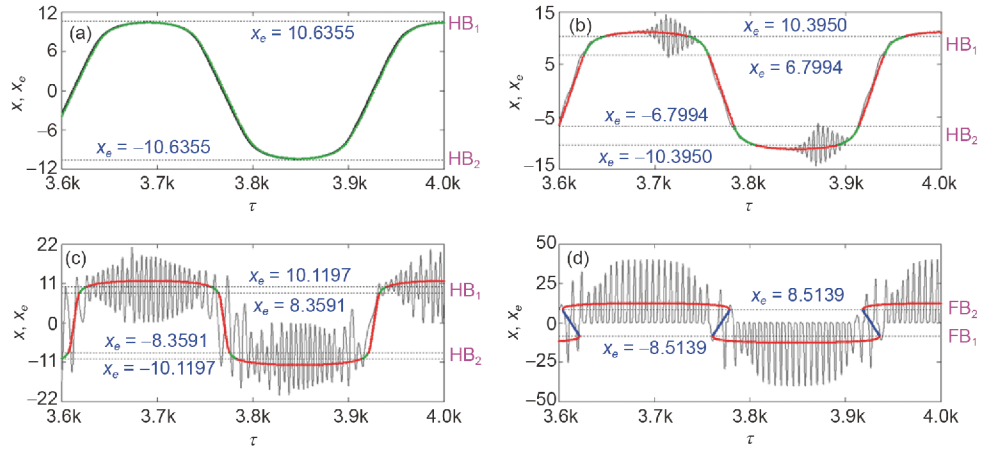

Figure 5 (Color online) Numerically simulated time series of x (the black lines) and x_e (the color lines) for l=0.667. (a) Periodic spiking at k_r=−0.6; (b) periodic bursting at k_r=−0.72; (c) chaotic spiking at k_r=−0.9; (d) chaotic spiking at k_r=−1.3.

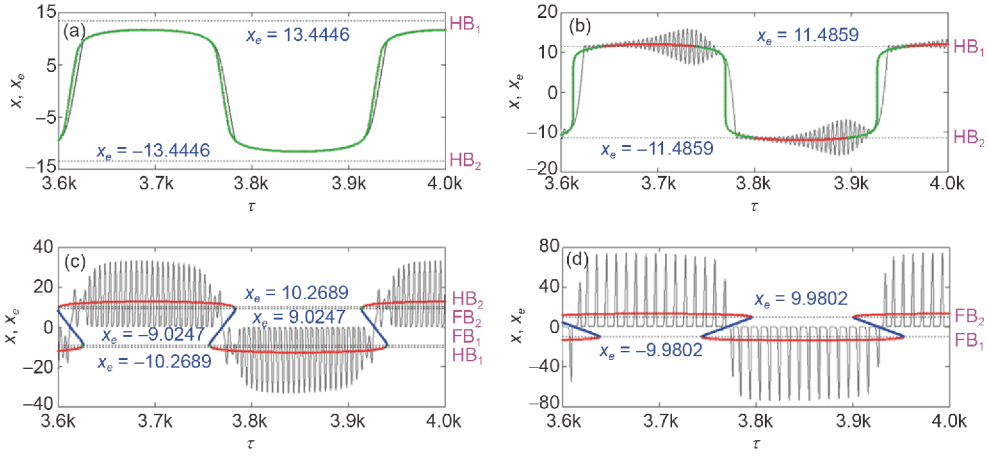

Figure 6 (Color online) Numerically simulated time series of x (the black lines) and x_e (the color lines) for l=3. (a) Periodic spiking at k_r=−0.85; (b) periodic bursting at k_r=−1.0; (c) periodic spiking at k_r=−1.5; (d) chaotic spiking at k_r=−2.3.

verified by eq. (18). These critical points are marked as H_1 ($\hat{H}_1$), H_4($\hat{H}_4$), H_2($\hat{H}_2$), and H_3($\hat{H}_3$), respectively, as seen in Figure 7.

It is well illustrated that the activity of system (4) alternates between the resting states within $H_1 \rightarrow H_4$, $\hat{H}_4 \rightarrow \hat{H}_1$ and spiking states within $A \rightarrow H_1$, $H_4 \rightarrow \hat{H}_4$, $\hat{H}_1 \rightarrow B$. The spiking states appear via HBs at H_4 and $\hat{H}_1$, and then vanish through HBs at H_1 and $\hat{H}_4$. Specially, in the middle region of the resting state, i.e. $H_2 \rightarrow H_3$ ($\hat{H}_3 \rightarrow \hat{H}_2$), the AC equilibrium points turns into the unstable index-2 saddle-foci via HB at H_2 ($\hat{H}_3$), but only small amplitude oscillations are observed from the time series of x and z, which may be caused by the

slow passage effect [48–50]. Afterwards, through Sub-HB at H_3 ($\hat{H}_2$), the small amplitude oscillation sustains until it reaches the HB point at H_4 ($\hat{H}_1$). Consequently, this kind of bursting activity is regarded as a Hopf/SubHopf burster [36]. Since the trajectory passes each HB points twice in a full busting period, the transitions between the resting and spiking states are hard to be distinguished from the overlapped transformed phase portrait depicted in Figure 7(b), but are clearly illustrated by the time series given in Figure 7 (a).

When k_r=−1.0/−1.2 and l=3 are considered, two periodic bursting activities with negative largest Lyapunov exponents are uncovered. The time series of x, z and x_e are presented in Figure 8(a1) and (b1) to clarify the transitions of the oscillation states. The corresponding transformed phase portraits are depicted in Figure 8(a2) and (b2), respectively. The periodic and chaotic bursting activities are briefly distinguished based on their time-domain waveforms and the calculated largest Lyapunov exponent. They can also be rigorously distinguished using 0–1 test [51,52].

For k_r=−1.0 and l=3, there are two HB points, as shown in Figure 8(a). Based on eq. (16), these two HB points are calculated to be (w, x)=(∓5.8595, ±11.4859) and marked as H_1($\hat{H}_1$) and H_2($\hat{H}_2$), respectively. The upper spiking state of the bursting activity is initiated through HB at H_1 and lasts until the trajectory reaches $\hat{H}_1$. Through HB at $\hat{H}_1$, E_{AC} turns from the unstable idex-2 saddle-focus (indicated by red lines) into the stable node-focus (indicated by green lines) and system (4) converts into the resting state. In the meantime, the trajectory moves to the lower oscillation region,

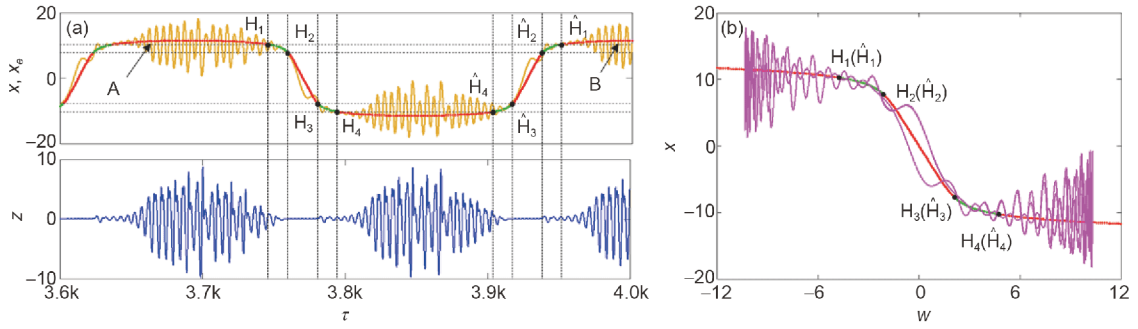

Figure 7 (Color online) Hopf/SubHopf chaotic bursting with k_r=−0.8 and l=0.667. (a) Time series of x, x_e, and z; (b) transformed phase portrait in the w-x plane overlapped with the trajectory of E_{AC}. In E_{AC} trajectories and time series of x_e, the red and green colors represent unstable index-2 saddle-focus and stable node-focus, respectively.

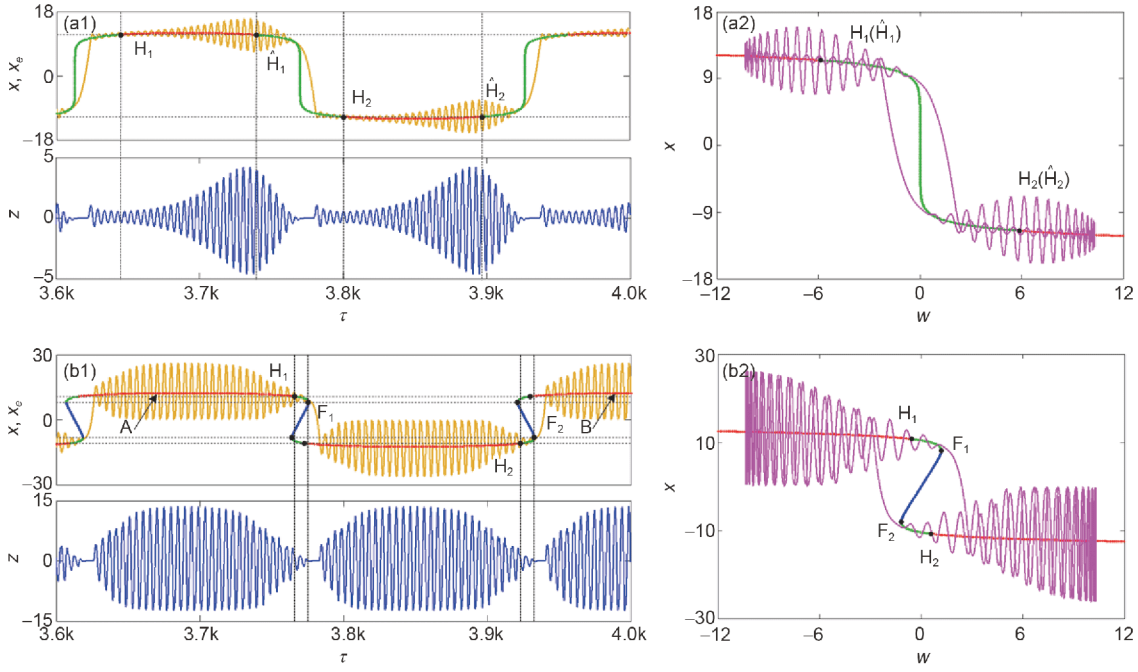

Figure 8 (Color online) Hopf/Hopf and Hopf-fold periodic bursting activities with k_r=−1.0/−1.2 and l=3, where (a1), (b1) are the time series of x, z, and x_e, and (a2), (b2) are the transformed phase portraits in the w-x plane overlapped with the E_{AC} trajectory. (a) k_r=−1.0; (b) k_r=−1.2. In the E_{AC} trajectories and time series of x_e, the red, blue and green colors represent unstable index-2 saddle-focus, unstable index-1 saddle-focus, and stable node-focus, respectively.

thereby completing half of the bursting loop. Similarly, the lower spiking state emerges via HB at H_2 and fades away through HB at $\hat{H}_2$. Thus, the bursting pattern of Figure 8(a) is classified as a Hopf/Hopf burster [36].

While for k_r=−1.2 and l=3, two HBs points located at (w, x) =(∓0.5795, ±10.7646) and two FB points located at (w, x)= (±1.1847, ±8.1084) are founded in the time series of x_e and E_{AC} trajectory. These points are marked as H_1, H_2, F_1, and F_2, respectively, as shown in Figure 8(b). Starting from point A, the system orbit follows along the upper branch of the E_{AC} trajectory and exhibits spiking state until it arrives at H_1. On this point, a short-term resting state appears via HB and disappears via FB at the nearby point F_1. Meanwhile, the system orbit jumps to the lower branch, initiating another spiking state around the unstable lower branch E_{AC} trajectory. Similarly, the lower-branch system orbit switches from the spiking state to the resting state via HB at H_2 and reverses back to the upper branch through FB at F_2. Accordingly, a Hopf/fold periodic bursting [36] is observed in system (4), which is somewhat similar to that reported in a memristive Wien-bridge oscillator with the same memristor emulator [40].

5 Hardware experiments

According to the circuit schematics in Figure 1, a breadboard

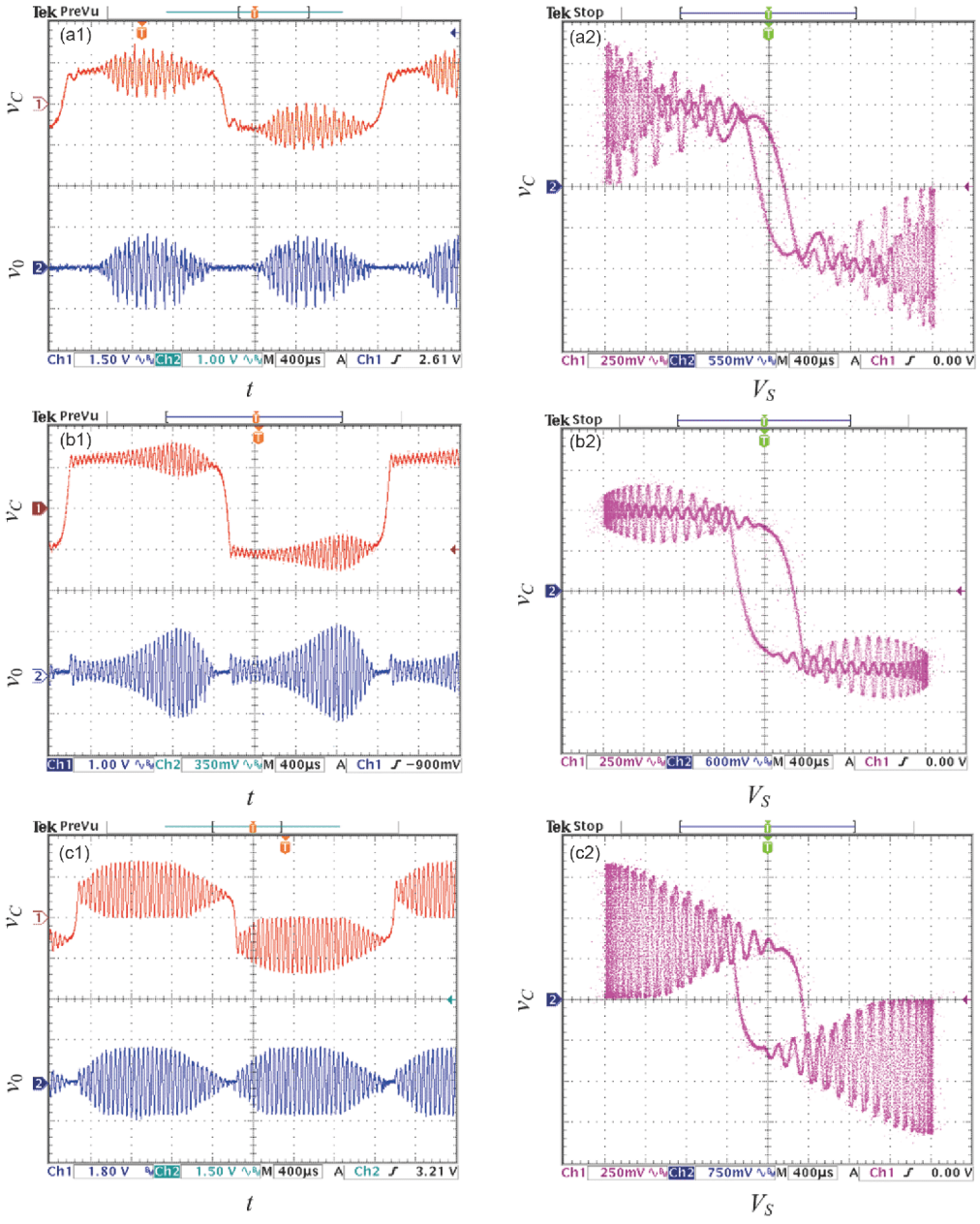

Figure 9 (Color online) Experimentally measured chaotic and bursting activities, where (a1)–(c1) are the time series of v_C and v_0, (a2)–(c2) are the transformed phase portraits in V_S-v_C plane. (a) R_1=−0.82 kΩ and L=14.47 mH; (b) R_1=−0.57 kΩ and L=3.23 mH; (c) R_1=−0.46 kΩ and L=3.23 mH.

experimental circuit is fabricated. An AD711KN operational amplifier with voltage supplies of ±15 V linked with three precision potentiometers is used to implement the negative resistor R_1. Four 1N4148 diodes cascaded with a manually winding inductor and a ceramic capacitor are utilized to construct the second-order memristive diode bridge emulator. The AC voltage source is obtained from a signal generator. The experimental results are measured by a digital oscilloscope.

When the circuit parameters are measured as V_m=1 V, f=0.32 kHz, C=9.95 nF, C_0=3.21 nF, L=14.47 mH, L_0=5.3 mH, R=1 kΩ, and R_1=−0.82 kΩ, the time series of v_C and v_0 as well as transformed phase portrait in V_S-v_C plane are captured in Figure 9(a). Meanwhile, when two adjustable circuit parameters are determined as R_1=−0.57 kΩ and L=3.23 mH, the corresponding time series and transformed phase portrait are obtained in Figure 9(b). Furthermore, when the circuit parameters are tuned as R_1=−0.46 kΩ and L=3.23 mH, the results of the time series and transformed phase portrait are given in Figure 9(c). Compared Figure 9 with Figures 7 and 8, the results in Figure 9(a) agree with those in Figure 7, whereas the results in Figure 9(b) and (c) coincide with those in Figure 8(a) and (b), respectively.

Neglecting the circuit parameter migrations caused by the limited accuracy of element values, parasitic parameters of the experimental circuits, and the measuring errors, the experimental results in Figure 9 can confirm that this non-autonomous memristive FHN circuit indeed exhibits various kinds of bursting activities.

6 Conclusion

In this paper, a memristive non-autonomous FHN circuit was constructed using a second-order memristive diode bridge emulator. The external forcing term was implemented using an AC voltage source to achieve physical realizability. When the exciting term was specified as a single slowly varying variable, periodic and chaotic bursting activities were observed in the memristive FHN circuit. As a non-autonomous system, these bursting activities were innovatively classified based on the time series of the AC equilibrium points and state variables. With this consideration, the bursting activities via Hopf/subHopf, Hopf/Hopf, and Hopf/fold bifurcations were identified in the specified parameter regions. Besides, the experimental measurements were performed to verify the numerically simulated results. The analytical understandings and hardware experimental investigations of the single memristive FHN circuit may contribute to design, investigation and application of artificial neural networks [53,54]. Particularly, from the viewpoint of the AC equilibrium points, qualitative analyses for dynamics in non-autonomous systems can be readily performed. It provides a novel perspective for related investigations of non-autonomous systems.

This work was supported by the National Natural Science Foundation of China (Grant Nos. 61601062, 51777016, 61801054 & 51607013), the Natural Science Foundation of Jiangsu Province, China (Grant No. BK20191451), and the Postgraduate Research & Practice Innovation Program of Jiangsu Province, China (Grant No. KYCX19_1764).

1 Duan L X, Lu Q S, Wang Q Y. Two-parameter bifurcation analysis of firing activities in the Chay neuronal model. Neurocomputing, 2008, 72: 341–351
2 Alidousti J, Ghaziani R K. Spiking and bursting of a fractional order of the modified FitzHugh-Nagumo neuron model. Math Model Comput Simul, 2017, 9: 390–403
3 Ma J, Tang J. A review for dynamics in neuron and neuronal network. Nonlinear Dyn, 2017, 89: 1569–1578
4 Hodgkin A L, Huxley A F. A quantitative description of membrane current and its application to conduction and excitation in nerve. J Physiol, 1952, 117: 500–544
5 Hindmarsh J L, Rose R M. A model of the nerve impulse using two first-order differential equations. Nature, 1982, 296: 162–164
6 Wang H X, Wang Q Y, Zheng Y H. Bifurcation analysis for Hindmarsh-Rose neuronal model with time-delayed feedback control and application to chaos control. Sci China Tech Sci, 2014, 57: 872–878
7 Morris C, Lecar H. Voltage oscillations in the barnacle giant muscle fiber. Biophys J, 1981, 35: 193–213
8 Xu L F, Li C D, Chen L. Contrastive analysis of neuron model. Acta Phys Sin, 2016, 65: 240701
9 Fitzhugh R. Impulses and physiological states in theoretical models of nerve membrane. Biophys J, 1961, 1: 445–466
10 Nagumo J, Arimoto S, Yoshizawa S. An active pulse transmission line simulating nerve axon. Proc IRE, 1962, 50: 2061–2070
11 Baltanás J P, Casado J M. Bursting behaviour of the FitzHugh-Nagumo neuron model subject to quasi-monochromatic noise. Physica D, 1998, 122: 231–240
12 Abbasian A H, Fallah H, Razvan M R. Symmetric bursting behaviors in the generalized FitzHugh-Nagumo model. Biol Cybern, 2013, 107: 465–476
13 Vaidyanathan S. Global chaos control of the FitzHugh-Nagumo chaotic neuron model via integral sliding mode control. Int J Pharm-Tech Res, 2016, 9: 413−425
14 Li F, Liu Q, Guo H, et al. Simulating the electric activity of Fitzhugh-Nagumo neuron by using Josephson junction model. Nonlinear Dyn, 2012, 69: 2169–2179
15 Guo Y F, Wang L J, Wei F, et al. Dynamical behavior of simplified FitzHugh-Nagumo neural system driven by Lévy noise and Gaussian white noise. Chaos Soliton Fract, 2019, 127: 118–126
16 Wang Z, Campbell S A. Symmetry, Hopf bifurcation, and the emergence of cluster solutions in time delayed neural networks. Chaos, 2017, 27: 114316
17 Saha A, Feudel U. Extreme events in FitzHugh-Nagumo oscillators coupled with two time delays. Phys Rev E, 2017, 95: 062219
18 Shepelev I A, Vadivasova T E, Bukh A V, et al. New type of chimera structures in a ring of bistable FitzHugh-Nagumo oscillators with nonlocal interaction. Phys Lett A, 2017, 381: 1398–1404
19 Masoliver M, Masoller C. Sub-threshold signal encoding in coupled FitzHugh-Nagumo neurons. Sci Rep, 2018, 8: 8276
20 Hu M, Li H, Chen Y R, et al. Memristor crossbar-based neuromorphic computing system: A case study. IEEE Trans Neural Netw Learning Syst, 2014, 25: 1864–1878
21 Sheridan P M, Cai F X, Du C, et al. Sparse coding with memristor networks. Nat Nanotech, 2017, 12: 784–789
22 Wang Z R, Li C, Song W Y, et al. Reinforcement learning with analogue memristor arrays. Nat Electron, 2019, 2: 115–124

23 Ge M Y, Jia Y, Xu Y, et al. Mode transition in electrical activities of neuron driven by high and low frequency stimulus in the presence of electromagnetic induction and radiation. Nonlinear Dyn, 2018, 91: 515–523
24 Zhang G, Wang C N, Alzahrani F, et al. Investigation of dynamical behaviors of neurons driven by memristive synapse. Chaos Soliton Fract, 2018, 108: 15–24
25 Du L, Cao Z L, Lei Y M, et al. Electrical activities of neural systems exposed to sinusoidal induced electric field with random phase. Sci China Tech Sci, 2019, 62: 1141–1150
26 Ma J, Mi L, Zhou P, et al. Phase synchronization between two neurons induced by coupling of electromagnetic field. Appl Math Comput, 2017, 307: 321–328
27 Njitacke Z T, Kengne J. Complex dynamics of a 4D Hopfield neural networks (HNNs) with a nonlinear synaptic weight: Coexistence of multiple attractors and remerging Feigenbaum trees. AEU-Int J Electron Commun, 2018, 93: 242–252
28 Bao H, Liu W B, Hu A H. Coexisting multiple firing patterns in two adjacent neurons coupled by memristive electromagnetic induction. Nonlinear Dyn, 2019, 95: 43–56
29 Lv M, Ma J, Yao Y G, et al. Synchronization and wave propagation in neuronal network under field coupling. Sci China Tech Sci, 2019, 62: 448–457
30 Mvogo A, Takembo C N, Ekobena Fouda H P, et al. Pattern formation in diffusive excitable systems under magnetic flow effects. Phys Lett A, 2017, 381: 2264–2271
31 Ma J, Zhang G, Hayat T, et al. Model electrical activity of neuron under electric field. Nonlinear Dyn, 2019, 95: 1585–1598
32 Zhang J H, Liao X F. Effects of initial conditions on the synchronization of the coupled memristor neural circuits. Nonlinear Dyn, 2019, 95: 1269–1282
33 Zhang J H, Liao X F. Synchronization and chaos in coupled memristor-based FitzHugh-Nagumo circuits with memristor synapse. AEU-Int J Electron Commun, 2017, 75: 82–90
34 Bao H, Liu W B, Chen M. Hidden extreme multistability and dimensionality reduction analysis for an improved non-autonomous memristive FitzHugh-Nagumo circuit. Nonlinear Dyn, 2019, 96: 1879–1894
35 Chen M, Qi J W, Xu Q, et al. Quasi-period, periodic bursting and bifurcations in memristor-based FitzHugh-Nagumo circuit. AEU-Int J Electron Commun, 2019, 110: 152840
36 Izhikevich E M. Neural excitability, spiking and bursting. Int J Bifurcat Chaos, 2000, 10: 1171–1266
37 Guo D Q, Wu S D, Chen M M, et al. Regulation of irregular neuronal firing by autaptic transmission. Sci Rep, 2016, 6: 26096
38 Lu L L, Jia Y, Xu Y, et al. Energy dependence on modes of electric activities of neuron driven by different external mixed signals under electromagnetic induction. Sci China Tech Sci, 2019, 62: 427–440
39 Zhang Z D, Li Y Y, Bi Q S. Routes to bursting in a periodically driven oscillator. Phys Lett A, 2013, 377: 975–980
40 Wu H G, Bao B C, Liu Z, et al. Chaotic and periodic bursting phenomena in a memristive Wien-bridge oscillator. Nonlinear Dyn, 2016, 83: 893–903
41 Bi Q S, Li S L, Kurths J, et al. The mechanism of bursting oscillations with different codimensional bifurcations and nonlinear structures. Nonlinear Dyn, 2016, 85: 993–1005
42 Chen X K, Li S L, Zhang Z D, et al. Relaxation oscillations induced by an order gap between exciting frequency and natural frequency. Sci China Tech Sci, 2017, 60: 289–298
43 Bao B C, Wu P Y, Bao H, et al. Symmetric periodic bursting behavior and bifurcation mechanism in a third-order memristive diode bridge-based oscillator. Chaos Soliton Fract, 2018, 109: 146–153
44 Han C Y, Yu S M, Wang G Y. A sinusoidally driven lorenz system and circuit implementation. Math Probl Eng, 2015, 2015: 706902
45 Xu Q, Zhang Q L, Qian H, et al. Crisis-induced coexisting multiple attractors in a second-order nonautonomous memristive diode bridge-based circuit. Int J Circ Theor Appl, 2018, 46: 1917–1927
46 Zhao H T, Lin Y P, Dai Y X. Hopf bifurcation and hidden attractor of a modified Chua's equation. Nonlinear Dyn, 2017, 90: 2013–2021
47 Xue W, Qi G Y, Mu J J, et al. Hopf bifurcation analysis and circuit implementation for a novel four-wing hyper-chaotic system. Chin Phys B, 2013, 22: 080504
48 Desroches M, Kaper T J, Krupa M. Mixed-mode bursting oscillations: Dynamics created by a slow passage through spike-adding canard explosion in a square-wave burster. Chaos, 2013, 23: 046106
49 Premraj D, Suresh K, Banerjee T, et al. An experimental study of slow passage through Hopf and pitchfork bifurcations in a parametrically driven nonlinear oscillator. Commun Nonlinear Sci Numer Simul, 2016, 37: 212–221
50 Wu H G, Ye Y, Chen M, et al. Extremely slow passages in low-pass filter-based memristive oscillator. Nonlinear Dyn, 2019, 97: 2339–2353
51 Gottwald G A, Melbourne I. On the implementation of the 0–1 test for chaos. SIAM J Appl Dyn Syst, 2009, 8: 129–145
52 Savi M A, Pereira-Pinto F H I, Viola F M, et al. Using 0–1 test to diagnose chaos on shape memory alloy dynamical systems. Chaos Soliton Fract, 2017, 103: 307–324
53 Rauber P E, Fadel S G, Falcao A X, et al. Visualizing the hidden activity of artificial neural networks. IEEE Trans Vis Comput Graph, 2016, 23: 101–110
54 Wang Z, Joshi S, Savel'ev S, et al. Fully memristive neural networks for pattern classification with unsupervised learning. Nat Electron, 2018, 1: 137–145